The expression of mantle seismic anisotropy in the global seismic wavefield

Jonathan Wolf[1,*], Maureen D. Long[1], Daniel A. Frost[3], Tarje Nissen-Meyer[2]

Abstract

The dependence of seismic wavespeeds on propagation or polarization direction, called seismic anisotropy, is a relatively direct indicator of mantle deformation and flow. Mantle seismic anisotropy is often inferred from measurements of shear-wave splitting. A number of standard techniques to measure shear-wave splitting have been applied globally; for example, *KS splitting is often used to measure upper mantle anisotropy. In order to obtain robust constraints on anisotropic geometry, it is necessary to sample seismic anisotropy from different directions, ideally using different seismic phases with different incidence angles. However, many standard analysis techniques can only be applied for certain epicentral distances and source-receiver geometries. In this work, we apply a "wavefield differencing" approach to (systematically) understand what parts of the seismic wavefield are most affected

*Corresponding author

Email address: jonathan.wolf@yale.edu (Jonathan Wolf)

[1]Department of Earth and Planetary Sciences, Yale University, New Haven, CT, USA

[2]Department of Earth Sciences, University of Oxford, Oxford, UK

[3]School of the Earth, Ocean and Environment, University of South Carolina, Columbia, SC, USA

by seismic anisotropy in the mantle. We systematically analyze differences between synthetic global wavefields calculated for isotropic and anisotropic input models, incorporating seismic anisotropy at different depths. Our results confirm that the seismic phases that are commonly used in splitting techniques are indeed strongly influenced by mantle anisotropy. However, we also identify less commonly used phases whose waveforms reflect the effects of anisotropy. For example, PS is strongly affected by upper mantle seismic anisotropy. We show that PS can be used to fill in gaps in global coverage in shear wave splitting datasets (for example, beneath ocean basins). We find that PcS is also a promising phase, and present a proof-of-concept example of PcS splitting analysis across the contiguous United States using an array processing approach. Because PcS is recorded at at much shorter distances than *KS phases, PcS splitting can therefore fill in gaps in backazimuthal coverage. The insights provided by a wavefield differencing approach provide promising new strategies for improving our ability to detect and characterize seismic anisotropy in the mantle.

Keywords: Numerical modelling, Seismic anisotropy, Planetary interiors, Computational seismology, Wave propagation

1. Introduction

Mantle deformation induced by convective mantle flow manifests itself in seismic anisotropy (e.g., Long and Becker, 2010). Seismic anisotropy denotes the dependence of seismic wavespeeds on the propagation or polarization direction of the wave. It has been demonstrated that seismic anisotropy is particularly strong in the boundary layers of mantle convection, while it is

almost absent in the bulk of the lower mantle (Panning and Romanowicz, 2006). In particular, seismic anisotropy has been detected in the upper mantle (e.g., Silver, 1996; Savage, 1999; Becker and Lebedev, 2021), the mantle transition zone (e.g., Yuan and Beghein, 2014; Chang and Ferreira, 2019), the uppermost lower mantle (e.g., Foley and Long, 2011; Lynner and Long, 2015; Mohiuddin et al., 2015; Chang and Ferreira, 2019; Ferreira et al., 2019), and the lowermost mantle (e.g., Wookey et al., 2005; Nowacki et al., 2010; Creasy et al., 2017; Wolf et al., 2019; Lutz et al., 2020; Wolf and Long, 2022). In general, the deeper seismic anisotropy is located in the mantle, the more difficult it is to resolve it with body wave approaches (Wolf et al., 2022a). Despite the challenges, however, a thorough picture of mantle anisotropy across all depths would be helpful to understand global patterns of mantle deformation and flow (e.g., Becker and Lebedev, 2021).

Seismic anisotropy manifests itself in the seismic wavefield in a number of ways, and there are several analytical techniques used to detect and characterize it. Anisotropy in Earth's crust and upper mantle can be measured using receiver function analysis (e.g., Levin and Park, 1997; Schulte-Pelkum et al., 2005; Nikulin et al., 2009; Wirth and Long, 2012) or surface wave tomography (e.g., Panning and Nolet, 2008; Ferreira et al., 2010; Zhu et al., 2020). Waveform inversion techniques have also been developed to characterize radial anisotropy in the mantle (e.g., Kawai and Geller, 2010; Suzuki et al., 2021). Probably the most commonly used method to study seismic anisotropy in Earth's mantle invokes measurements of so-called shear-wave splitting (e.g., Long and Silver, 2009). The distribution of shear wave energy away from its initial polarization direction, splitting the wave into two

quasi-shear waves, is indicative of seismic anisotropy (Silver and Chan, 1991).

Depending on which portion of the mantle is being studied, different shear phases (or combinations of phases) are typically used. Figure 1a summarizes most commonly used seismic phases for the analysis of mantle anisotropy using shear wave splitting. To analyze seismic anisotropy in the upper mantle directly beneath the receiver, the most commonly used phase is SKS, sometimes supplemented with SKKS and PKS (e.g., Silver and Chan, 1991; Chevrot, 2000; Liu et al., 2014; Walpole et al., 2014; Graw and Hansen, 2017; Lopes et al., 2020). For such an analysis of upper mantle anisotropy, it is often assumed that the influence of lowermost mantle anisotropy is negligible. An alternative and commonly applied approach to studying upper mantle anisotropy is to infer source-side anisotropy from splitting of teleseismic S waves using explicit receiver-side anisotropy corrections (e.g., Russo and Silver, 1994; Lynner and Long, 2013; Walpole et al., 2017; Eakin et al., 2018). Source-side direct S splitting can also be used to study transition zone and uppermost lower mantle anisotropy in places where deep earthquakes occur (e.g., Foley and Long, 2011; Mohiuddin et al., 2015). These observational strategies are well-established and have been used to map upper mantle anisotropy across much of Earth's landmasses. Beneath the oceans, however, shear wave splitting constraints on upper mantle anisotropy are sparse (e.g., IRIS DMC, 2012), due to the paucity of seismic receivers.

Lowermost mantle anisotropy is generally more challenging to measure than seismic anisotropy in the upper mantle. A major reason for this is that all seismic waves that may sample seismic anisotropy in the lowermost mantle also travel through the upper mantle, potentially accumulating an upper

mantle splitting signal before they reach the station (Figure 1a). Different measurement strategies have been developed to distinguish between an upper and lowermost mantle contribution. Such techniques include the analysis of differential S-ScS splitting (e.g., Wookey et al., 2005; Nowacki et al., 2010; Creasy et al., 2017; Wolf et al., 2019), and differential splitting of SKS and SKKS (e.g., Niu and Perez, 2004; Deng et al., 2017; Grund and Ritter, 2018; Reiss et al., 2019; Tesoniero et al., 2020; Asplet et al., 2020). An alternative technique makes use of the long raypath of S_{diff} through the lowermost mantle, inferring deep mantle anisotropy by measuring splitting of S_{diff} (e.g., Vinnik et al., 1995; Cottaar and Romanowicz, 2013; Wolf and Long, 2022, 2023a; Wolf et al., 2023b), typically comparing with SKS splitting to account for any upper mantle contributions.

While the commonly used shear wave splitting techniques continue to yield valuable information on anisotropy at various depths in the mantle, they all have limitations, including those imposed by the distribution of seismic stations and earthquakes at the relevant distance ranges. Expanding the repertoire of seismic body wave phases that can be used for shear wave splitting analysis is desirable, as this would allow for splitting datasets with better spatial and azimuthal coverage. In service of this goal, in this study we carry out a systematic investigation of how seismic anisotropy located at different depths in the Earth's mantle expresses itself in the global seismic wavefield. To do this, we implement a wavefield differencing approach that compares synthetic wavefields calculated for isotropic and anisotropic input models. We analyze a large number of body wave phases (Figure 1), some of which are commonly used in shear wave splitting studies, but many

of which are not. We explore models that include anisotropic layers over a range of mantle depths (Figure 2), including the shallow upper mantle, the deep upper mantle, the transition zone, the uppermost lower mantle, and the D″ layer, which denotes the lowermost $200 - 300$ km of the mantle. The wavefield differencing approach allows us to systematically analyze the effects of anisotropy on the entire seismic wavefield, to investigate which phases are most sensitive to anisotropy in which portions of the mantle, and to identify non-standard phases that can potentially be incorporated in future shear wave splitting studies. In particular, our results point towards potential new (or rarely used) techniques to map upper mantle anisotropy, including those that rely on PS and PcS phases. We provide proof of concept examples of these strategies applied to real data and discuss how they might improve our ability to image anisotropy, deformation, and flow in the Earth's mantle.

2. Wavefield differencing: Methods and approach

2.1. Global wavefield simulations

We conduct global wavefield simulations using AxiSEM3D (Leng et al., 2016; 2019), which is capable of handling any three-dimensional input model and arbitrary seismic anisotropy (Tesoniero et al., 2020). In this work, we focus on axisymmetric simulations, for which AxiSEM3D is as efficient as its older relative AxiSEM (Nissen-Meyer et al., 2014). We compute global wave propagation simulations down to $\sim$5 s period using AxiSEM3D, following the methodology applied in previous work (e.g., Wolf et al., 2022b). We always use a smoothed version of isotropic PREM (Dziewonski and Anderson, 1981; see below) as our background model and always consider (PREM-) attenu-

ation as well as Earth's ellipticity. We intentionally keep our input models simple to generally assess where in the seismic wavefield seismic anisotropy manifests itself. Effects of laterally changing seismic anisotropy and three-dimensional input models have been addressed in previous work (e.g., Wolf et al., 2022b, 2023b).

The typical source-receiver configuration for our simulations is shown in Figure 2a. We place our 100 m deep seismic source at the North pole, simulating either a normal or strike-slip fault earthquake (Figure 2a). The very shallow focal depth helps to avoid surface reflections (depth phases) in our seismograms. We select two different focal mechanisms (Figure 2a); their details are only important inasmuch as they influence the initial polarization of the seismic wave. The stations are spaced on a regular 2-degree latitude-longitude grid, leading to a closer station spacing at the poles than at the equator (Figure 2a). This configuration ensures that stations are regularly spaced along the azimuthal direction. We implement seismic anisotropy in our models by replacing the smoothed PREM velocity input model by seismic anisotropy described by a horizontally transversely isotropic (HTI) elastic tensor created using MSAT (Walker and Wookey, 2012). We consider five different models, each with anisotropy in a different depth range. The depth ranges of anisotropy that we investigate are 24-220 km (layer 1), 220-400 km (layer 2), 400-670 km (layer 3), 670-800 km (layer 4) and 2641-2891 km (layer 5), as shown in Figure 2b. We ensure that the isotropic average of the anisotropy used in each of these layers agrees with our smoothed isotropic PREM model, for which velocities are constant within each layer. The anisotropic strength within our lowermost mantle layer (layer 5) is 2.75 %; we adjust

the anisotropic strength in each of the other layers such that we would obtain the same splitting delay time (∼1 s) for each of them for a vertically incident wave. We implement two different elastic tensor arrangements (Figure 2c,d), representing crystallographic preferred orientation of olivine: in one, the direction from which the elastic tensor is sampled changes with azimuth (arrangement 1; Figure 2c), while in the other it is always the same (arrangement 2; Figure 2d). We implement these two different elastic tensor arrangements to ensure that our results are not strongly affected by the specific direction that the seismic anisotropy is sampled from. Whenever we use the seismograms to calculate $absAD$ and $relAD$ (see below), we cannot output seismograms for all stations from our source-station setup (Figure 2a) at an appropriate sampling period (1 s) due to storage limitations. Instead, we output seismograms every 15° azimuth and every 2° distance.

2.2. Data processing

In order to understand how seismic anisotropy expresses itself, we compare the seismic wavefield computed for our isotropic input model with the wavefields from each of our anisotropic simulations. Specifically, we compute the displacement U_i or $\mathbf{U}$, the gradient of displacement D_{ij} or $\mathbf{D}$, the curl of displacement R_i or $\mathbf{R}$, stress S_{ij} or $\mathbf{S}$, and strain E_{ij} or $\mathbf{E}$, where i,j = 1,2,3 correspond to the radial (1), transverse (2) and vertical (3) direction. The difference between the isotropic and the anisotropic simulations will be indicated with a δ-sign in the following, for example $\delta U_1 = U_{1,iso} - U_{1,ani}$. From this differential wavefield, we infer how much different seismic phases are influenced by mantle anisotropy. We can express this either in terms of a scalar quantity that explicitly considers the amplitude of the incom-

ing wave, or as a scalar quantity that is normalized to the amplitude. To do this, we derive the phase-specific **abs**olute and **rel**ative normalized integrated **a**pparent **d**ifference ($absAD$ and $relAD$) from the delta field. For U_1 and the SS seismic phase $absAD$ can be expressed as:

$$absAD_{U_1,SS} = \sum_{a=0^\circ}^{180^\circ} \sum_{d=d1>20^\circ}^{d2\leq 180^\circ} \sum_{t=tSS}^{tSS+20} |\delta\Big(U_1^{a,d,t}\Big)|/(d2-d1) \ , \tag{1}$$

where a denotes the azimuth index, $d1$ is the shortest distance at which the phase arrives (but always $> 20^\circ$), $d2$ is the largest distance at which the phase arrives (but always $\leq 180^\circ$), d is the distance index, tSS is the phase arrival time for the SS phase, and t the time index. Therefore, $absAD$ quantifies how much a particular phase is influenced by mantle anisotropy by analyzing the 20 s after the predicted arrival time, integrating over distance and azimuth and normalizing the value by the distance range over which the phase occurs. Similarly, it can be calculated how much a particular phase is affected by mantle anisotropy relative to its isotropic amplitude. This quantity is

$$relAD_{U_1,SS} = \sum_{a=0^\circ}^{180^\circ} \sum_{d=d1>20^\circ}^{d2\leq 180^\circ} \Big(\max\Big(\Big|U_{iso}^{d,t=1,2,\ldots,20}\Big|\Big)\Big)^{-1} \sum_{t=tSS}^{tSS+20} |\delta\Big(U_1^{d,t}\Big)|/(d2-d1) \ , \tag{2}$$

where U_{iso} denotes the displacement amplitude in the isotropic seismogram. $absAD$ and $relAD$ will also be calculated for D_{ij}, R_i, S_{ij} and E_{ij} in addition to displacement U_{ij}.

For the interpretation of $absAD$ and $relAD$, it is important to note that

we do not explicitly consider phase interference in the calculations, but simply use the 20 s after the phase arrivals whether or not another seismic phase arrives in this time window. Moreover, the contribution to $absAD$ is stronger at shorter distances as $|\delta U_i|$ will be larger due to geometric spreading. This is not the case for $relAD$. Therefore, phases for which $absAD$ is large likely have large amplitudes for at least a certain distance range and are, at the same time, sensitive to seismic anisotropy. Phases for which $relAD$ is large do not necessarily have high amplitudes but are strongly indicative of seismic anisotropy.

3. Wavefield differencing results

To visualize the difference in seismic wave propagation between isotropic and anisotropic simulations, we create movies showing its time evolution. Example snapshots from such movies are shown in Figure 3 for seismic anisotropy in the upper mantle (upper panel) and the lowermost mantle (lower panel). We also provide Supplementary Movies S1-S5 that show the time evolution of the differential wavefield for elastic tensor arrangement 1 and seismic anisotropy at different depths (layers 1-5). The overall wavefield difference is substantially more affected by upper mantle anisotropy due to its influence on surface waves. The influence of surface waves becomes less the deeper in the mantle the seismic anisotropy is placed. In the difference snapshots for lowermost mantle anisotropy, different body wave phases that are often used to characterize it can be very well distinguished (e.g., SKS, SKKS, ScS, S_{diff}). The patterns that are apparent for upper and lowermost mantle anisotropy on a wavefront along a particular distance away from the source

are a combination of the initial source polarization and the sampling of the elastic tensor from an azimuth-dependent direction (arrangement 1).

While these wavefield difference movies are informative, they mainly visually emphasize the phase arrivals that are most affected by mantle seismic anisotropy at each point in time. To also focus on less affected phases, we investigate the differential wavefield at a particular azimuth, plotted on top of a travel time curve (Figure 4 for upper mantle and transition zone; Figure 5 for the lower mantle). Figure 4 demonstrates that, as expected, the deeper the anisotropy is placed in the upper mantle, transition zone, or uppermost lower mantle (layers 1-4), the weaker its influence on near surface reverberations and on surface waves. Phases that are strongly influenced by seismic anisotropy in layers 1 to 4 include, for example, SS, SSS and SSSS; in fact, these phases are affected so strongly that the difference plots show their minor arc siblings as features with an opposite moveout (upper right corner).

These results for layers 1-4 can be compared to those for layer 5 (lowermost mantle anisotropy; Figure 5). The magnitude of the wavefield differences depends on azimuth, but the absolute sensitivity of each seismic phase to lowermost mantle anisotropy is the same for all azimuths. Seismic phases that are primarily influenced by lowermost mantle anisotropy include the phases commonly used to infer its presence (e.g., ScS, S_{diff}, SK(K)S), but also ScSScS and ScSScSScS. Moreover, at certain distances (P)PS seems to be influenced by lowermost mantle anisotropy, likely because it is sampling the lowermost mantle at these distances and merging with (P)PScS (analogous to S/ScS at $\sim 90 - 100°$). The details of the differential wavefield

(unsurprisingly) depend on the focal mechanism and the elastic tensor arrangement (Supplementary Figures S1-S4). The overall patterns, however, are the same for all of these scenarios.

Next, we calculate $absAD$ (Equation (1)) for various seismic phases, which shows us how strongly absolute phase amplitudes are affected by mantle anisotropy. These results are shown for δU_i in Figure 6 and for D_{ij}, R_i, S_{ij} and E_{ij} in the Supplementary Figures S5-S13. As expected from the patterns in Figures 4 and 5, similar phases are affected by seismic anisotropy in layers 1 to 4, whereas the phases mainly influenced by lowermost mantle anisotropy (layer 5) are different. Figure 4 shows results for layers 1 to 4 for a given backazimuth, while Figure 5 shows results for lowermost mantle anisotropy and different backazimuths (0°, 30°, 60°, 90°), illustrating that while the details of the wavefield difference vary as a function of backazimuth, the seismic phases that are mainly affected by seismic anisotropy stay the same. It is unsurprising that S, SS, SSS and SSSS are strongly affected by upper mantle anisotropy since they travel through the upper mantle two or more times. We find that the transverse components (U_2) of SK(K)S phases are particularly affected by mantle anisotropy. This is expected since SK(K)S would be SV-polarized in an isotropic Earth due to the P-SV conversion at the CMB. Indeed, this insight underpins the popularity of SK(K)S splitting as a tool for measuring anisotropy. The fact that PKIKS and PKS seem largely unaffected by mantle anisotropy in this view has to do with the strike-slip focal mechanism used for the simulation (compare to Supplementary Figure S6); this is therefore a function of the radiation pattern, rather than an actual lack of sensitivity to anisotropy.

Our calculation of $absAD$ for different phases can shed light on whether there are body wave phases that are strongly affected by mantle anisotropy that are not typically used in splitting studies. Such phases, which are strongly affected by seismic anisotropy in layers 1-4 in all simulations (Figure 6a-d, Supplementary Figures S5-S13) include PS and PPS. This is especially noteworthy because their polarization is determined by the P-SV conversion through of the surface underside reflection, which makes them much easier to analyze than, for example, SS. We also find that PcS is strongly influenced by upper mantle anisotropy in our simulations. This is partially due to the interference with S at some of the distance range, but in general, PcS splitting is analogous to *KS splitting, although PcS usually has smaller amplitudes (e.g., Liu and Grand, 2018). For the lowermost mantle case, we find that anisotropy mostly affects SKS, SKKS and ScS phases (Figure 6e) and no unusual phases that are strongly affected by deep mantle anisotropy, but rarely used to infer its presence, are immediately apparent.

So far, we have analyzed how much seismic phases are affected by mantle anisotropy in terms of absolute amplitude. Results for relative amplitude or $relAD$ are shown in Figure 7 for δU_i. Figure 7 shows that for each layer, transverse components are particularly affected for phases that travel through the outer core and convert from P to SV at the CMB. This is logical because in the isotropic case transverse component energy is not present in the absence of phase interference. (Note that to avoid dividing by zero, we add a water level divisor to our calculations). Seismic anisotropy in layers 1-4 tends to affect S, SS, SSS and SSSS increasingly strongly, since the higher multiples sample seismic anisotropy more often. For the lowermost mantle,

prominent signals for PKS and ScSScS are visible for $relAD$ which were less apparent for $absAD$ in Figure 5e.

4. Novel splitting strategies based on wavefield differencing results

4.1. Differential PS-SKS splitting: inferring upper mantle anisotropy close to the PS reflection point

We demonstrated in Section 3 that PS waves are strongly affected by seismic anisotropy in Earth's upper layers. For the purpose of splitting measurements, which are only sensitive to anisotropy structure along the path, PS is initially SV-polarized due to the P-to-S conversion upon reflection at the surface. It is worth pointing out that, because for the measurement of shear wave splitting an S arrival at the receiver is needed, the order of S and P is generally not reversible (e.g, we could not measure SP splitting). On the S-leg of the raypath, PS samples seismic anisotropy in the upper mantle close to the reflection point as well as beneath the seismic receiver, and at distances between 90° and 115° any potential influence of lowermost mantle anisotropy can be avoided. Beneath the station, SKS samples seismic anisotropy in a very similar way as PS, such that differential PS-SKS splitting would point towards upper mantle anisotropy close to the PS reflection point at the surface (analogous to SKS-SKKS differential splitting for the lowermost mantle). Su and Park (1994) invoked this argument and measured seismic anisotropy in a location beneath the southwestern Pacific Ocean; however, this strategy has apparently not been used since. One possible reason for this is that there is no advantage to using the PS-SKS differential splitting technique when the alternative is to infer upper mantle anisotropy close to the poten-

tial reflection point by directly measuring SKS splitting at a seismic station located there. However, seismic stations are not regularly distributed across Earth's surface. Differential PS-SKS splitting is therefore potentially helpful to study anisotropy in regions that are sampled by PS bounce points but are not themselves well instrumented.

Here we present a proof-of concept example of PS-SKS splitting using real data. Before measuring PS and SKS splitting, we bandpass-filter our data, retaining periods between 6 and 25 s. To analyze seismic anisotropy, we use SplitRacer (Reiss and Rümpker, 2017), a MATLAB-based graphical user interface. SplitRacer calculates the following shear wave splitting parameters: the fast polarization direction measured relative to north (ϕ), the time delay between the fast and the slow quasi S wave (δt), and the splitting intensity (SI; Chevrot, 2000) of the split wave. To measure the first two quantities, SplitRacer uses the transverse energy minimization technique (Silver and Chan, 1991) along with a corrected error formulation by Walsh et al. (2013). A strength of SplitRacer is that time windows are picked automatically, thereby ensuring that measurements are independent of a specific choice of time window.

We demonstrate a proof-of-concept example for PS-SKS splitting using station INK (Walpole et al., 2014) located in northeastern Canada, which exhibits null or nearly null SKS splitting over the entire backazimuthal range. Since INK is a null station, any splitting contribution to PS waves must be caused by seismic anisotropy on the raypath far away from the station, most likely close to the PS reflection point at the surface. We analyze PS splitting parameters for events that occurred in the southeastern Pacific subduction

zones between 10/1995 and 01/2023 at distances between 90° and 115°. Our results are shown in Figure 8. We obtain ∼100 robust splitting intensity and two robust (ϕ, δt) measurements. We identify a strongly anisotropic region in the upper mantle to the north of Fiji, in which fast polarization directions are oriented approximately south-north (Figure 8d). The PS waveforms and splitting diagnostic plots of the event (2009-01-19 03:35:18) are shown in Figure 8a-c; this event was used to infer the (ϕ, δt) values for this strongly anisotropic region. Figure 8a shows a clearly split PS phase, while the SKS phase for the same event is null. After correcting for the best-fitting PS splitting parameters (Figure 8c), the corrected particle motion is linear (Figure 8b), as expected in case of splitting due to seismic anisotropy.

Upper mantle anisotropy has been densely mapped beneath continents; however, for seismic anisotropy beneath ocean basins very little shear wave splitting data are available (IRIS DMC, 2012). To the extent that previous splitting measurements have been reported for the oceans, they were often made at ocean island stations (e.g., Fontaine et al., 2007), which themselves represent an anomalous tectonic setting, potentially influencing the upper mantle anisotropy beneath. Moreover, sometimes splitting measurements have been obtained through measurements of splitting from direct S waves (Mohiuddin et al., 2015; Eakin et al., 2018). Alternatively, some splitting measurements have been made using ocean bottom seismometers (e.g., Zietlow et al., 2014; Lynner, 2021), which are expensive to install and typically yield relatively noisy data. We therefore recommend that the differential PS-SKS splitting technique be used systematically to map upper mantle anisotropy beneath oceans. Motivated by the findings presented in this work,

we have applied this technique to map seismic anisotropy beneath the Pacific Ocean basin (Wolf and Long, 2023b).

4.2. PcS beam splitting: inferring upper mantle anisotropy near the receiver

Our results for $relAD$ (Figure 5) suggest that PcS is significantly affected by mantle seismic anisotropy. However, due to its usually low amplitudes, PcS is not commonly used for the purpose of splitting measurements, with a few exceptions (e.g., Murdie and Russo, 1999; He and Long, 2011). Here, we apply a recently established beamforming technique to increase PcS signal-to-noise ratios and to measure splitting from the resulting beams.

To beamform PcS phase arrivals, we follow the same methodology as Frost et al. (2020) and Wolf et al. (2023a), using data from an event that occurred on 08/24/2011 in the Peru-Brazil border region (Figure 9a). Wolf et al. (2023a) demonstrated that shear-wave splitting measurements from beamformed SK(K)S data reflect an average of the single-station splitting from the seismograms used for the beam. Therefore, PcS beam splitting is equivalent to a laterally averaged splitting contribution. Following Wolf et al. (2023a), we construct subarrays of between 10 and 20 stations across the contiguous United States, which have a size of approximately 3°x3°. For each subarray, we estimate slowness and backazimuth of the incoming wave, and use this information to calculate radial and transverse component beams from velocity seismograms that were bandpass-filtered retaining periods between 4 and 50 s. As suitable given the size of our subarrays, we use a curved wavefront approach instead of the typical plane-wave approximation (Rost and Thomas, 2009). To enhance slowness-backazimuth estimates, we measure how similar individual records are to the calculated beam, a quantity

known as the F-statistic (Selby, 2008; Frost et al., 2013). The maximum amplitude of the F-trace is used to infer the best-fitting slowness and back-azimuth values. To be able to fairly compare waveforms and amplitudes between different components, we then calculate the linearly stacked beam using these slowness and backazimuth values for the unfiltered data.

We measure PcS beam splitting using SplitRacer, analogously to how we use it for PS and SKS splitting. We first apply a bandpass filter to our beamformed data, retaining periods between 4-25 s (Figure 9d). This approach leads to robust splitting intensity measurements for most of the subarrays; however, we cannot obtain any well-constrained (ϕ, δt) measurements because splitting is generally weak, below the detection level for the transverse energy minimization method at these periods. However, the beamformed waveforms show clear PcS signals and relatively low noise levels. We therefore next measure splitting at frequencies that are higher than usual for shear wave splitting measurements, retaining periods between 1-10 s (Figure 9e). While the splitting intensity results are very similar to those obtained with the 4-25 s bandpass-filter, we successfully measure robust (ϕ, δt) splitting parameters for nine subarrays. The inclusion of higher frequency energy helps to resolve (ϕ, δt) because the time delay is larger compared to the dominant period of the signal. The measured (ϕ, δt) splitting parameters we obtain with this approach are similar to previously published *KS splitting measurements compiled in the IRIS shear wave splitting database IRIS DMC (2012).

Given this successful example, we suggest that PcS beam splitting measurements can be used in the future to fill in gaps in backazimuthal coverage

that often exist for *KS measurements. PcS is useful because it is recorded at shorter distances than *KS (up to $\sim$63°) and therefore can largely increase the number of usable seismic events. A region for which PcS beam splitting measurements might be particularly helpful to improve backazimuthal coverage is Japan, which also has a densely spaced seismic stations suitable for beamforming, and which suffers from poor backazimuthal coverage for SK(K)S (Long and van der Hilst, 2005). Further, we suggest that splitting measurements from beamformed data can generally be made at higher frequencies, which can increase the number of robust (ϕ, δt) measurements in cases of weak splitting, as shown in our example (Figure 9e). The use of phases such as PcS that are recorded at a shorter distance than *KS also potentially has the effect that less high frequency energy is lost through attenuation along the raypath.

5. Challenges and future directions

In this work, we have analyzed differences in the seismic wavefield between isotropic and anisotropic simulations of global seismic wave propagation. The results we obtained point towards new splitting strategies, two of which we demonstrated as proof-of-concept examples.

While additional new strategies can potentially be identified based on our modeling results, as discussed below, we face the challenge that some phases that may be strongly influenced by mantle anisotropy are complicated to analyze. As demonstrated in Section 3, S can be strongly influenced by upper mantle anisotropy. This is why S is often used to characterize anisotropy near the earthquake source (e.g., Russo and Silver, 1994; Foley and Long, 2011;

Walpole et al., 2017; Eakin et al., 2018). However, since there are limits to how reliable explicit corrections for receiver side anisotropy are (Wolf et al., 2022a), the technique should be applied with caution. S is relatively simple because it samples the upper mantle only twice (once on the downgoing leg near the source and once on the upgoing leg near the receiver). The phase SS, on the other hand, potentially samples upper mantle anisotropy four times: at the source side, twice close to the reflection point, and beneath the receiver. This renders the phase practically unusable for inferring the precise geometry of upper mantle anisotropy in any particular location, although this has been tried (e.g., Wolfe and Silver, 1998). Theoretically, upper mantle anisotropy should be known along three of the four legs of the raypath through the upper mantle to infer seismic anisotropy for the unknown leg, which is unrealistic for almost all possible source-receiver configurations. Alternatively, the sampled reflection point anisotropy could be assumed to be the same along the up- and downgoing leg for SS. Even if this assumption was justified, it would likely be practically impossible to reliably infer the anisotropy, at least using explicit ray-theory based corrections (Wolf et al., 2022a). This issue is applicable to any seismic phase that may be strongly influenced by mantle anisotropy and samples anisotropy in many separate locations. Therefore, while the splitting of phases such as SS, SSS etc. may provide a general indication of the presence of seismic anisotropy along the raypath, it is not well suited to studying the geometry of anisotropy in any given region.

To infer lowermost mantle seismic anisotropy, we usually face a similar challenge. All phases that potentially sample lowermost mantle anisotropy also potentially sample seismic anisotropy in the upper mantle, which has to

somehow be accounted for in studies of deep mantle anisotropy. Many of the phases that we have shown to be strongly influenced by lowermost mantle anisotropy (Section 3), are already often used to diagnose it. For example, SKS-SKKS differential splitting is common (e.g., Niu and Perez, 2004; Reiss et al., 2019), S and ScS are often analyzed together to infer lowermost mantle anisotropy (Wookey et al., 2005; Nowacki et al., 2010; Wolf et al., 2019), and S_{diff} waves are also commonly used to infer lowermost mantle anisotropy (e.g., Vinnik et al., 1989; Cottaar and Romanowicz, 2013; Wolf et al., 2023b). Our results do not clearly point to unusual phases that can be used to infer lowermost mantle anisotropy in future studies. While ScSScS unsurprisingly is strongly influenced by deep mantle anisotropy, it suffers from the same technical limitations as phases such as SS, SSS, etc., as discussed previously. Figure 5 shows that beyond around 120°, PS starts to be influenced by lowermost mantle anisotropy. However, it is unclear how this could be exploited in practice. In theory, a PS-PScS differential splitting technique could be applied in an analogous manner to S-ScS differential splitting. However, a complication is that PS and PScS do not generally have the same reflection point at the surface. Therefore, splitting close to the reflection point would be hard to characterize for PScS, making it impossible to distinguish it from a lowermost mantle contribution.

In order to accurately measure splitting due to mantle seismic anisotropy in a particular region of the mantle, the wave should (ideally) not sample seismic anisotropy in multiple different locations along the raypath. Additionally, to enable splitting analysis the initial polarization of the wave should be known. Both these conditions are satisfied for the two novel split-

ting strategies we explore here: PS-SKS differential splitting and PcS beam splitting. SKS, PS and PcS all involve initially SV-polarized S waves due to the P-SV conversion either at the CMB or at the surface. PcS phases do not usually have high amplitudes (Liu and Grand, 2018), which is why it is helpful to use these waves in a beamforming framework. We suggest that it is often more helpful to use seismic phases with lower amplitudes, for which it is straightforward to understand where along the raypath mantle anisotropy is sampled, than seismic phases that may be strongly influenced by mantle anisotropy, but in a complicated manner (for example, SS). Such low amplitude seismic phases can be enhanced using array techniques, making use of the fact that the splitting parameters measured from beams or stacks approximately agree with the average splitting parameters of the single-station seismograms contributing to them (Wolf et al., 2023a). Such an approach has been applied to S3KS previously (Wolf et al., 2023a) and to relatively high-frequency PcS in this work. Based on these findings, we suggest to apply beamforming routinely in studies that measure shear-wave splitting. For example, Figure 5 shows that there are minor arc seismic phases affected by lowermost mantle anisotropy. Such phases, like minor arc SKKS or S3KS, can be used for measurements of mantle anisotropy more commonly than they currently are. Similarly, the measurement of differential PPS-SKS or PPS-SKKS splitting is conceivable, by enhancing signals via beamforming if necessary. Such new splitting strategies involving minor arc phases and unusual source-receiver configurations will be helpful to infer upper mantle anisotropy in locations that suffer from poor coverage, as well as to study lowermost mantle anisotropy, which is often only detectable for specific raypath

configurations.

6. Conclusion

In this work, we have applied a wavefield differencing approach to analyze the differences between wavefield for isotropic and anisotropic models, incorporating seismic anisotropy at different mantle depths. These wavefield differencing results demonstrate which seismic phases are most strongly influenced by mantle anisotropy. We show that some seismic phases are more suitable than others to infer splitting parameters even if they are influenced by mantle anisotropy to a similar degree. In particular, we suggest that the PS-SKS differential splitting technique can be commonly used to infer upper mantle seismic anisotropy beneath ocean basins, based on a proof-of-concept example using a station in Canada and earthquakes in the western Pacific. Additionally, seismic phases that are not usually used for splitting measurements because of their low amplitudes should be more routinely analyzed in areas of dense seismic array deployments using a beamforming approach. As a proof-of-concept example, we calculate high-frequency PcS beam splitting for one seismic event for stations across the US. The wavefield differencing results presented here may inform the design of future studies of mantle anisotropy using body waves.

Data availability

The synthetic seismograms for this study were computed using AxiSEM3D, which is publicly available at `https://github.com/AxiSEMunity` (Leng et al., 2016; 2019).

The stations across the US used for beamforming of PcS have the following network codes: AR, AZ (UC San Diego, 1982), BK (Northern California Earthquake Data Center, 2014), CC (Cascades Volcano Observatory/USGS, 2001), CI (California Institute of Technology and United States Geological Survey Pasadena, 1926), CN (Natural Resources Canada (NRCAN Canada), 1975), CU (Albuquerque Seismological Laboratory (ASL)/USGS, 2006), EP, GS (Albuquerque Seismological Laboratory (ASL)/USGS, 1980), HW, II (Scripps Institution of Oceanography, 1986), IM, IU (Albuquerque Seismological Laboratory/USGS, 2014), IW (Albuquerque Seismological Laboratory (ASL)/USGS, 2003), LB, LD (Lamont Doherty Earth Observatory (LDEO), Columbia University, 1970), NE (Albuquerque Seismological Laboratory (ASL)/USGS, 1994), NM, PE (Penn State University, 2004), SC, TA (IRIS Transportable Array, 2003), UO (University of Oregon, 1990), US (Albuquerque Seismological Laboratory (ASL)/USGS, 1990), UW (University of Washington, 1963), XO (Gary Pavlis and Hersh Gilbert, 2011), Y5, YX (Simon Klemperer and Kate Miller, 2010), Z9 (Fischer et al., 2010). The station used for the PS splitting measurements is INK (Natural Resources Canada (NRCAN Canada), 1975). All data are publicly available.

Acknowledgements

This work was funded by Yale University and by the U.S. National Science Foundation via grant EAR-2026917 to MDL and grant EAR-2027181 to DAF. We thank the Yale Center for Research Computing for providing the necessary research computing infrastructure for this study. The Generic Mapping Tools (Wessel and Smith, 1998), ObsPy (Beyreuther et al., 2010),

MSAT (Walker and Wookey, 2012), SplitRacer (Reiss and Rümpker, 2017) and AxiSEM3D (Leng et al., 2016; 2019) were used in this research.

Figures

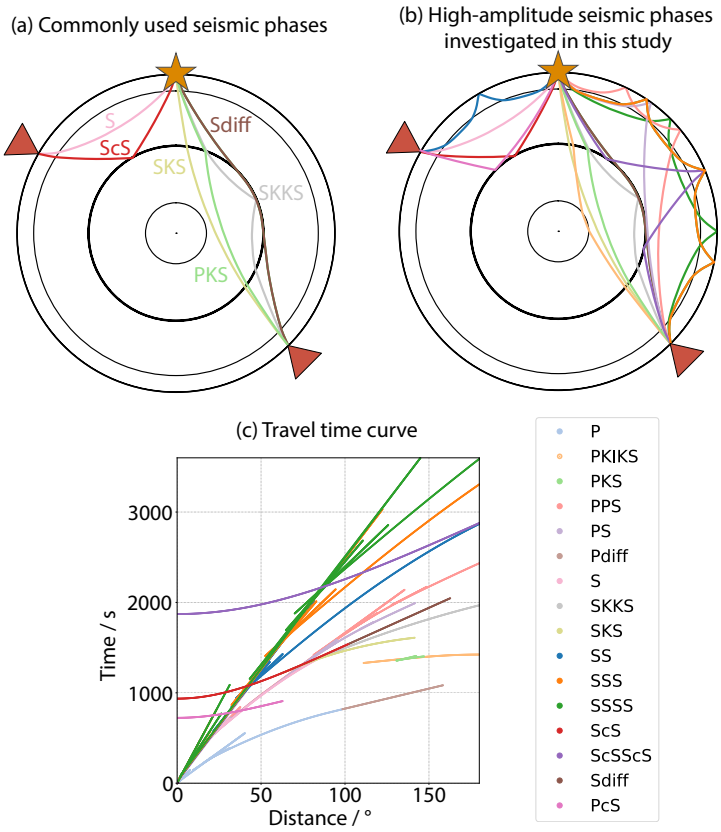

Figure 1: Seismic phases used and this study and their travel times. (a) Raypath sketch for seismic phases commonly used to infer upper (SKS, SKKS, PKS) and lowermost (SKS, SKKS, S, ScS, S_{diff}) mantle anisotropy. (b) Seismic phases that usually have high amplitudes in seismograms investigated in this study. See legend for color key. (c) Travel time curve for all seismic phases presented in panel (b), using the same colors. The travel time curve was calculated for a 100 m deep event, as used in the global wavefield simulations.

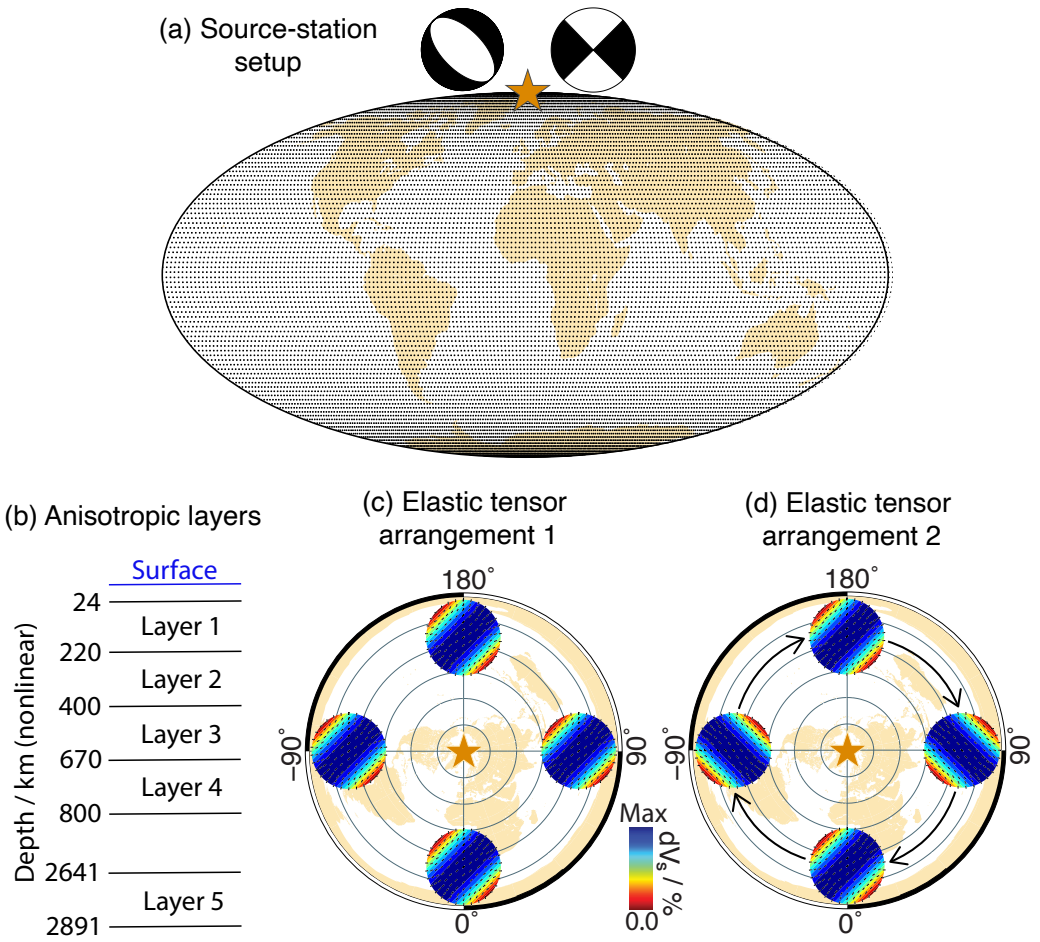

Figure 2: Setup for global wavefield simulations. (a) Source (yellow star) – station (black dots on map) configuration. Events either have a normal (left) or a strike-slip (right) geometry (top). (b) Depths at which we incorporate seismic anisotropy into our AxiSEM3D input models. Layer 1: Upper mantle; layer 2: lower upper mantle; layer 3: transition zone; layer 4: upper lower mantle; layer 5: lowermost mantle. (c) Elastic tensor arrangement 1. The source is represented as a yellow star on the map, which uses a north pole centered projection, and the horizontally transversely isotropic elastic tensors are shown as stereoplots. For elastic tensor arrangement 1, the direction from which the elastic tensor is sampled changes as a function of azimuth. (d) Elastic tensor arrangement 2, presented using the same plotting conventions as in panel (c). For elastic tensor arrangement 2, the direction from which the elastic tensor is sampled is the same for every azimuth.

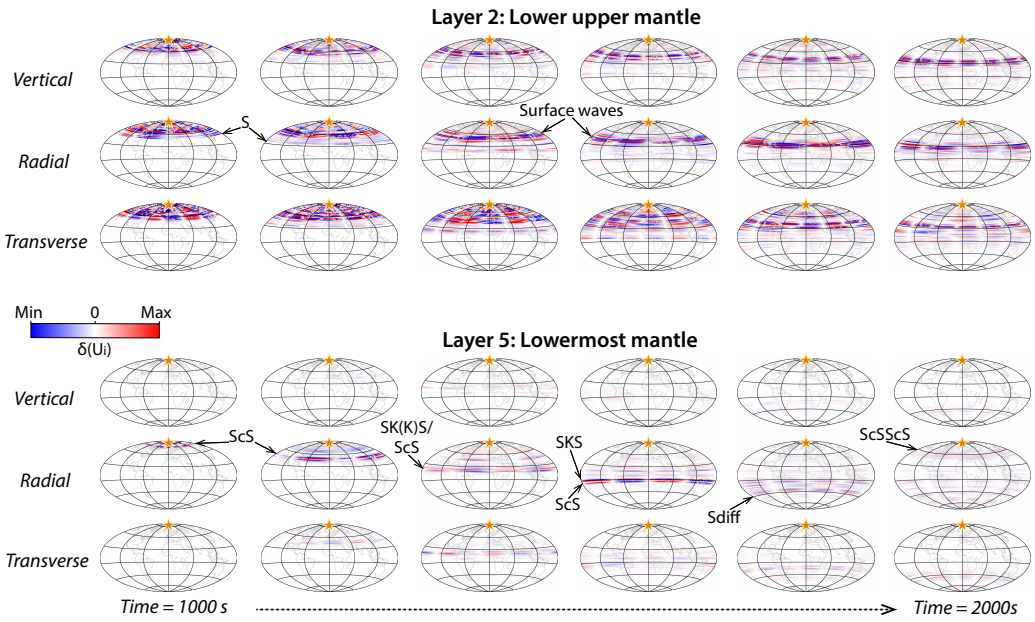

Figure 3: Time snapshots of the differential displacement wavefield (see color bar) for vertical, radial and transverse components from 1000 s (left) to 2000 s (right) after event origin time, for elastic tensor arrangement 1. The top panel shows δU_i for seismic anisotropy in the lower upper mantle and the bottom panel for the lowermost mantle. Different seismic phases are marked on the snapshots.

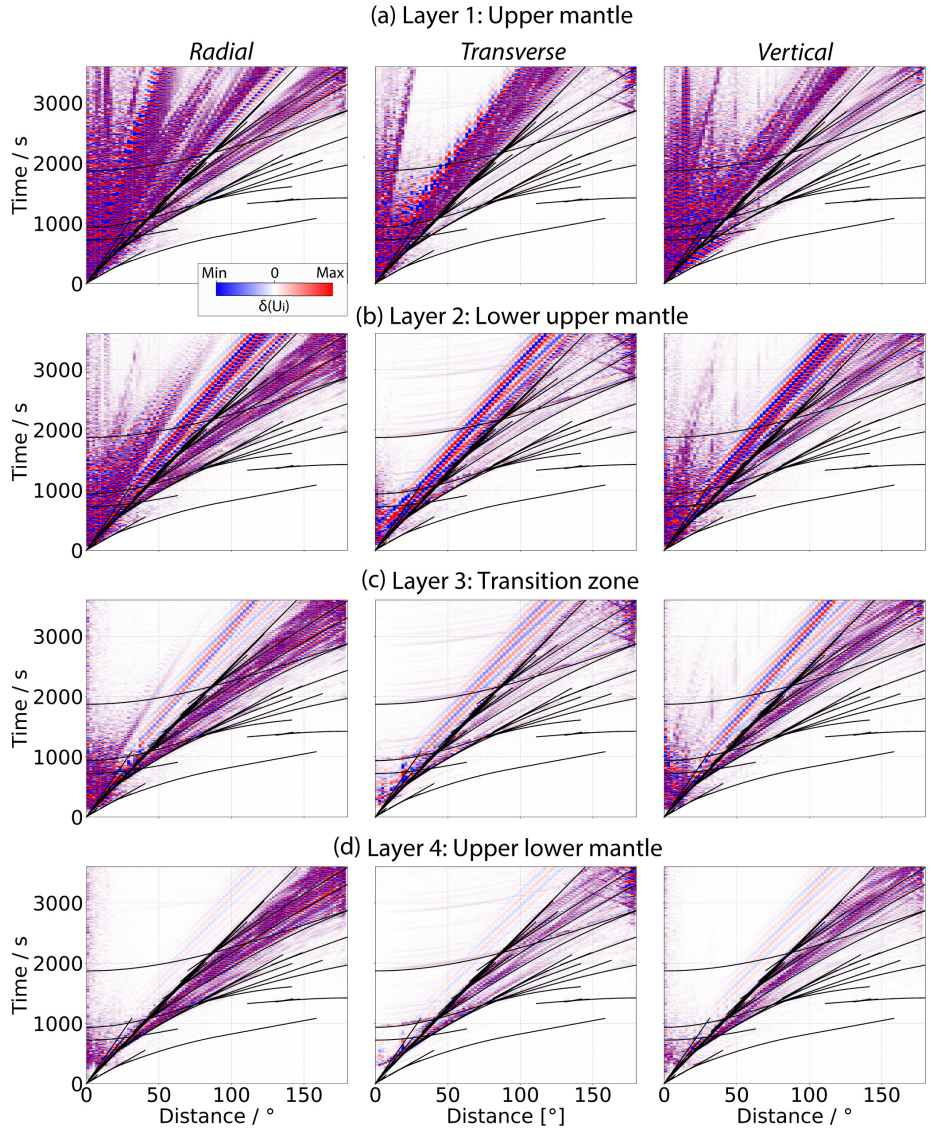

Figure 4: Differential displacement wavefield (color bar) as a function of distance for an azimuth of 0°, calculated using a strike-slip source and elastic tensor arrangement 1 (Figure 2c). (a) The differential wavefield for seismic anisotropy in layer 1 (upper mantle) is plotted underneath the travel time curve shown in Figure 1c with the phase travel times shown as black lines. The wavefield difference is presented for radial (left), transverse (middle) and vertical (right) components. (b) Same as panel (a) for seismic anisotropy in layer 2 (lower upper mantle). (c) Same as panel (a) for seismic anisotropy in layer 3 (transition zone). (d) Same as panel (a) for seismic anisotropy in layer 4 (upper lower mantle). White vertical stripes are due to the plotting convention are not to be interpreted.

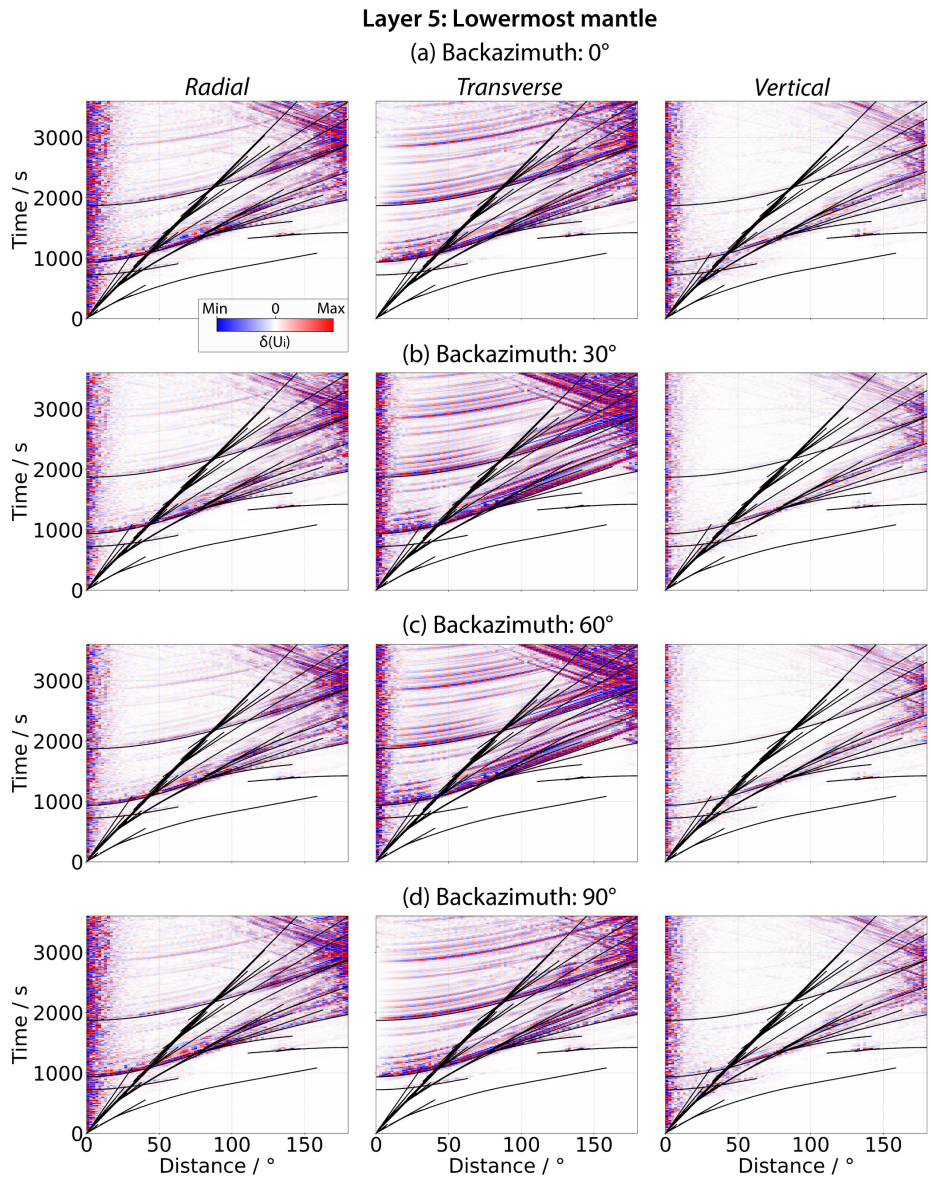

Figure 5: Differential displacement wavefield (color bar) as a function of distance for azimuths 0° (first row), 30° (second row), 60° (third row) and 90° (fourth row), calculated using a strike-slip source and elastic tensor arrangement 1 (Figure 2c) for lowermost mantle anisotropy. Plotting conventions are as in Figure 4.

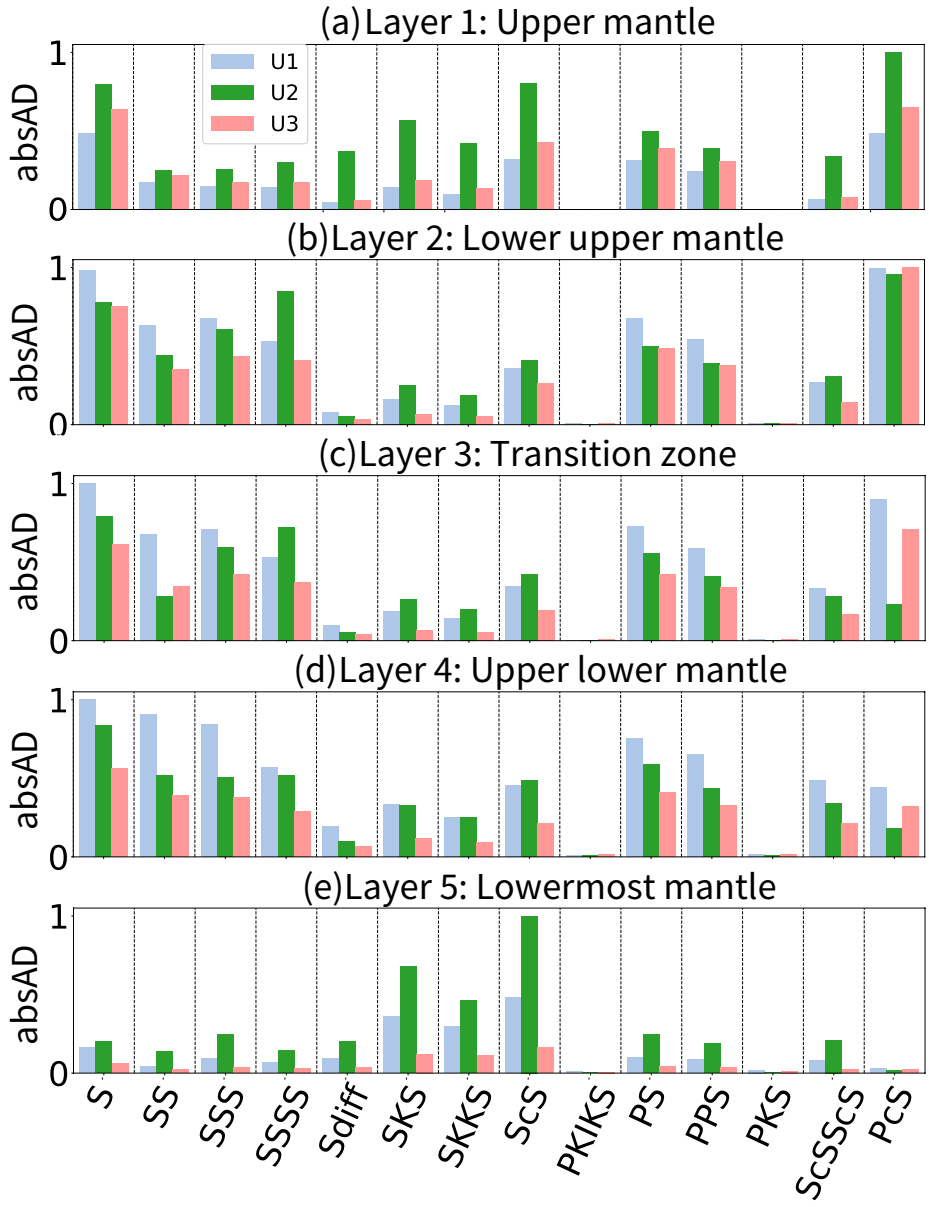

Figure 6: $absAD_{U_i}$ (see text) for radial (U_1, blue), transverse (U_2, green) and vertical (U_3, red) components for most seismic phases shown in Figure 1b. (a) $absAD_{U_i}$, normalized to the largest amplitude of either U_1, U_2 or U_3, for seismic anisotropy in layer 1 (upper mantle). b) Same as panel (a) for seismic anisotropy in layer 2 (lower upper mantle). (c) Same as panel (a) for seismic anisotropy in layer 3 (transition zone). (d) Same as panel (a) for seismic anisotropy in layer 4 (upper lower mantle). (e) Same as panel (a) for seismic anisotropy in layer 5 (lowermost mantle).

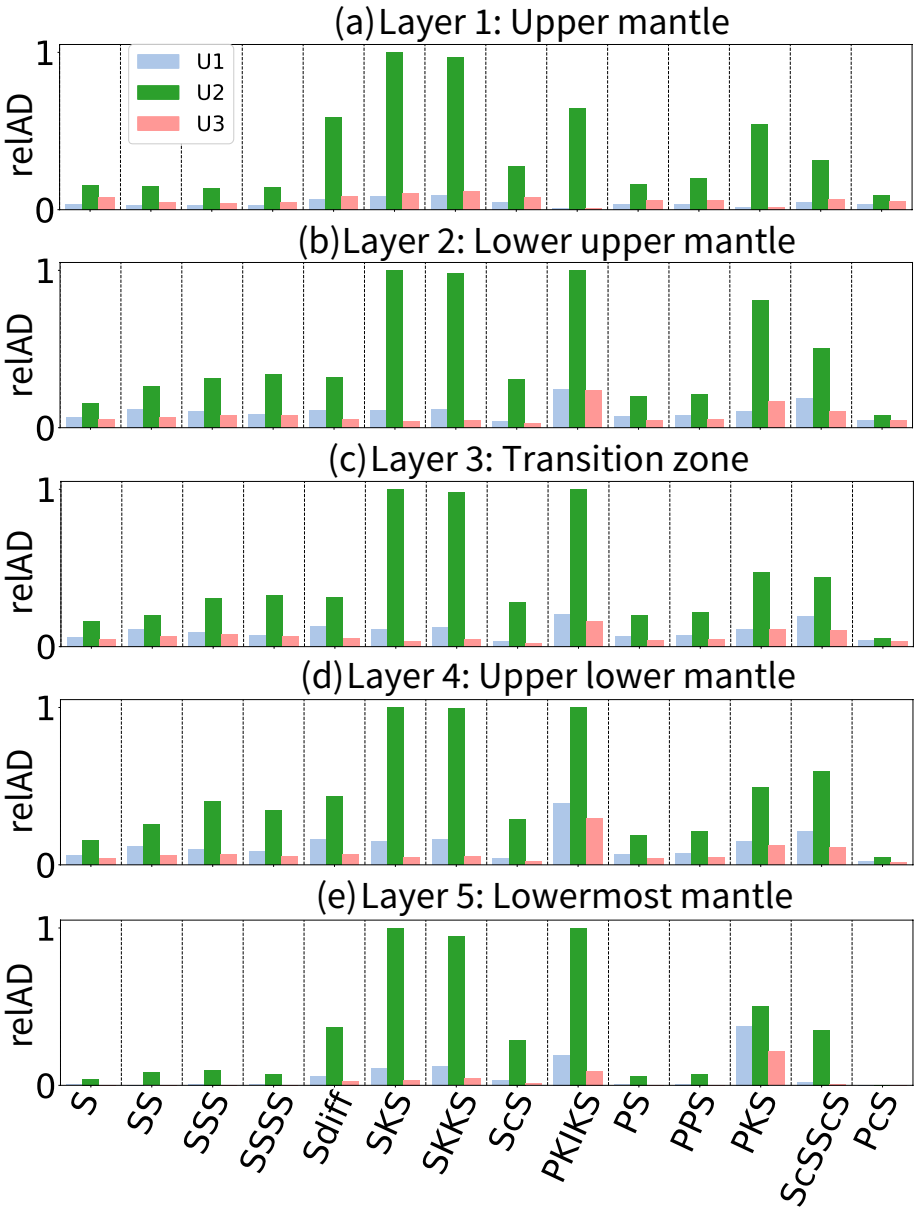

Figure 7: Same as Figure 6 for $relAD_{U_i}$.

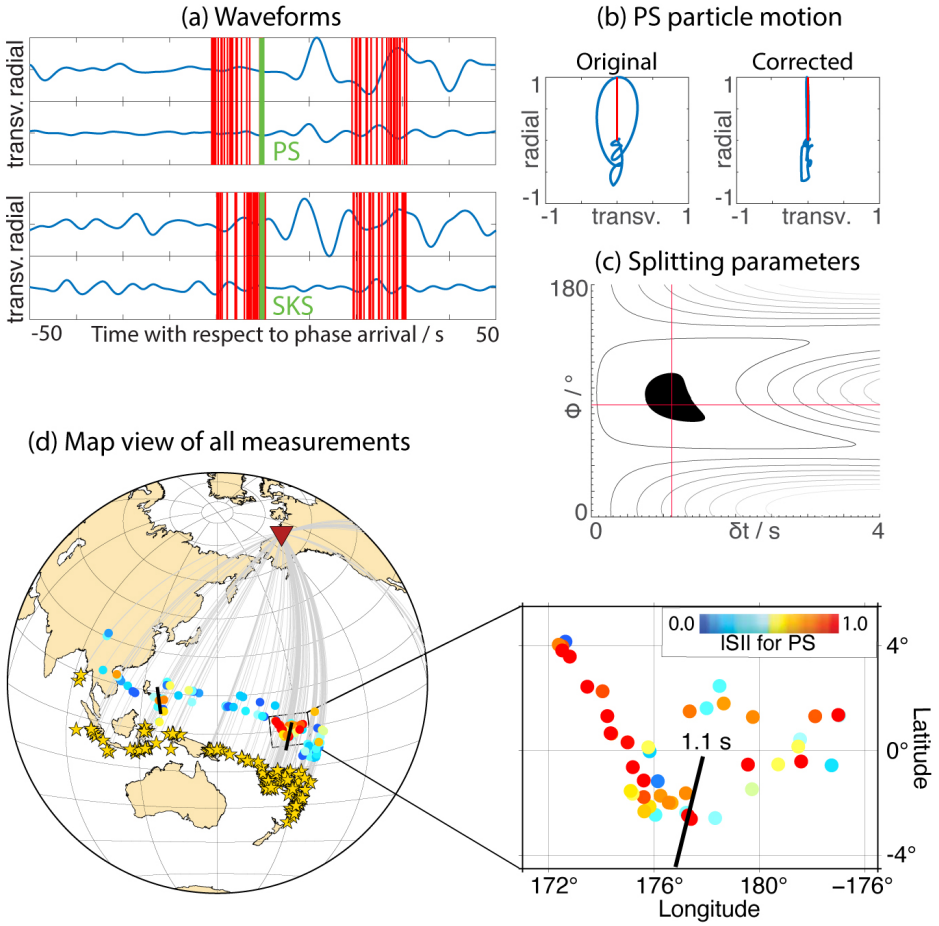

Figure 8: Differential PS-SKS splitting results for null station INK (Walpole et al., 2014). (a) PS (top) and SKS (bottom) radial and transverse component waveforms for an event that occurred on 01/19/2009. The PREM-predicted phase arrival time is shown with a green line and the start/end of the automatically selected measurement windows are shown with red lines. SKS transverse energy is at the amplitude level of the noise; therefore, SKS splitting is null. (b) PS particle motions before (left) and after (right) correcting for the best fitting splitting parameters. (c) Best-fitting splitting parameters in the ϕ-δt plane. The 95% confidence interval is shown in black, red crossing lines show the best fitting combination of (ϕ, δt). (d) Map view of the source (orange stars) – receiver (red triangle) configuration for the differential PS-SKS splitting analysis. Raypaths are shown as gray lines and colored circles indicate absolute PS splitting intensities (see legend). Black lines represent (ϕ, δt) splitting parameters. Bottom right: Zoom-in for the region of strong upper mantle anisotropy.

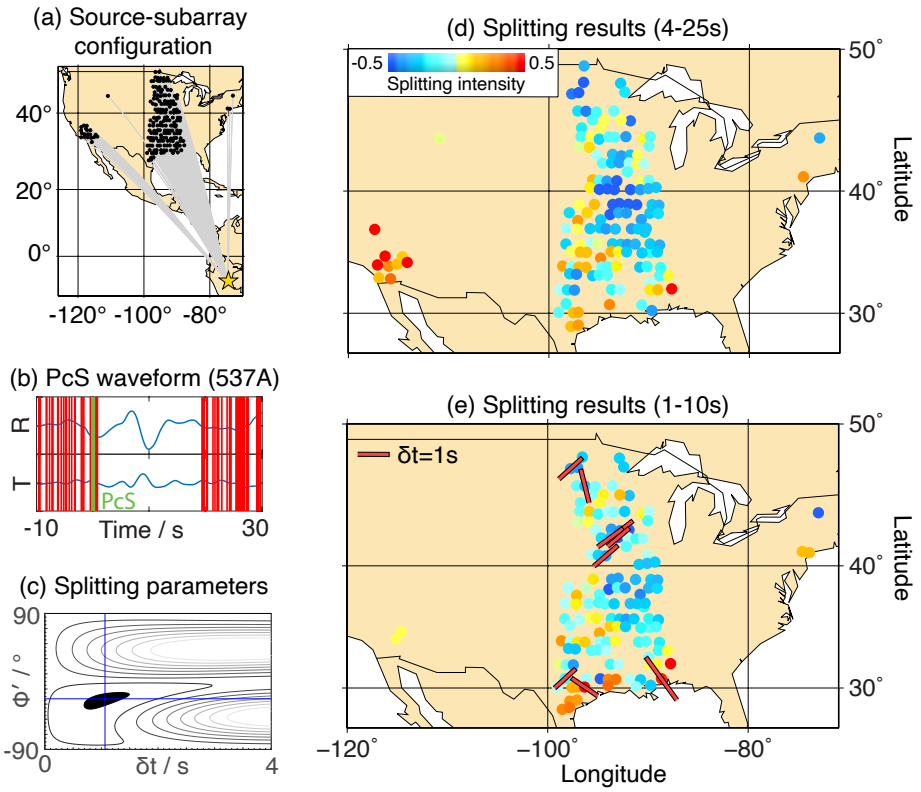

Figure 9: Summary of PcS beam splitting measurements. (a) The event used for the beamforming, which occurred on 08/24/2011, is represented as a yellow star (moment magnitude: 7.0; depth: 149 km). Subarray central stations across US are shown as black circles. (b) Radial (R) and transverse (T) component PcS beam waveforms for an example subarray with central station 537A. The PREM-predicted phase arrival time is shown by a green line and the start/end of the automatically selected measurement windows is presented by red lines. (c) Best fitting splitting parameters (ϕ', δt) for the waveforms shown in panel (b). ϕ' denotes the fast polarization direction measured clockwise from the backazimuthal direction. The 95% confidence interval is represented in black, with contour lines showing different transverse energy component levels. (d) Splitting measurements after applying a 4 to 25 s bandpass filter. Colors represent the splitting intensity (see legend), and are plotted a the central station location of each subarray. (e) Similar to panel (d) for a bandpass filter between 1 and 10 s. Nine well-constrained (ϕ, δt) measurements (red sticks) are obtained.

References

Albuquerque Seismological Laboratory (ASL)/USGS, 1980. Us geological survey networks. URL: https://doi.org/10.7914/SN/GS.

Albuquerque Seismological Laboratory (ASL)/USGS, 1990. United states national seismic network. URL: https://doi.org/10.7914/SN/US.

Albuquerque Seismological Laboratory (ASL)/USGS, 1994. New england seismic network. URL: https://doi.org/10.7914/SN/NE.

Albuquerque Seismological Laboratory (ASL)/USGS, 2003. Intermountain west seismic network. URL: https://doi.org/10.7914/SN/IW.

Albuquerque Seismological Laboratory (ASL)/USGS, 2006. Caribbean network. URL: https://doi.org/10.7914/SN/CU.

Albuquerque Seismological Laboratory/USGS, 2014. Global seismograph network (gsn - iris/usgs). URL: https://doi.org/10.7914/SN/IU.

Asplet, J., Wookey, J., Kendall, M., 2020. A potential post-perovskite province in D″ beneath the Eastern Pacific: evidence from new analysis of discrepant SKS–SKKS shear-wave splitting. Geophysical Journal International 221, 2075–2090. URL: https://doi.org/10.1093/gji/ggaa114.

Becker, T.W., Lebedev, S., 2021. Dynamics of the Upper Mantle in Light of Seismic Anisotropy. American Geophysical Union (AGU). chapter 10. pp. 257–282. URL: https://doi.org/10.1002/9781119528609.ch10.

Beyreuther, M., Barsch, R., Krischer, L., Megies, T., Behr, Y., Wassermann, J., 2010. Obspy: A python toolbox for seismology. Seismological Research

Letters 81, 530–533. URL: https://doi.org/10.1111/10.1785/gssrl.81.3.530.

California Institute of Technology and United States Geological Survey Pasadena, 1926. Southern california seismic network. URL: https://doi.org/10.7914/SN/CI.

Cascades Volcano Observatory/USGS, 2001. Cascade chain volcano monitoring. URL: https://doi.org/10.7914/SN/CC.

Chang, S.J., Ferreira, A.M.G., 2019. Inference on Water Content in the Mantle Transition Zone Near Subducted Slabs From Anisotropy Tomography. Geochemistry, Geophysics, Geosystems 20, 1189–1201. URL: https://doi.org/10.1029/2018GC008090.

Chevrot, S., 2000. Multichannel analysis of shear wave splitting. Journal of Geophysical Research: Solid Earth 105, 21579–21590. URL: https://doi.org/10.1029/2000JB900199.

Cottaar, S., Romanowicz, B., 2013. Observations of changing anisotropy across the southern margin of the African LLSVP. Geophysical Journal International 195, 1184–1195. URL: https://doi.org/10.1093/gji/ggt285.

Creasy, N., Long, M.D., Ford, H.A., 2017. Deformation in the lowermost mantle beneath Australia from observations and models of seismic anisotropy. Journal of Geophysical Research: Solid Earth 122, 5243–5267. URL: https://doi.org/10.1002/2016JB013901.

Deng, J., Long, M.D., Creasy, N., Wagner, L., Beck, S., Zandt, G., Tavera, H., Minaya, E., 2017. Lowermost mantle anisotropy near the eastern edge of the Pacific LLSVP: constraints from SKS-SKKS splitting intensity measurements. Geophysical Journal International 210, 774–786. URL: https://doi.org/10.1093/gji/ggx190.

Dziewonski, A.M., Anderson, D.L., 1981. Preliminary reference Earth model. Physics of the Earth and Planetary Interiors 25, 297–356. URL: https://doi.org/10.1016/0031-9201(81)90046-7.

Eakin, C., Rychert, C., Harmon, N., 2018. The Role of Oceanic Transform Faults in Seafloor Spreading: A Global Perspective From Seismic Anisotropy. Journal of Geophysical Research: Solid Earth 123, 1736–1751.

Ferreira, A., Faccenda, M., Sturgeon, W., Chang, S.J., Schardong, L., 2019. Ubiquitous lower-mantle anisotropy beneath subduction zones. Nature Geoscience 12, 301—-306. URL: https://doi.org/10.1038/s41561-019-0325-7.

Ferreira, A.M.G., Woodhouse, J.H., Visser, K., Trampert, J., 2010. On the robustness of global radially anisotropic surface wave tomography. Journal of Geophysical Research: Solid Earth 115. URL: https://doi.org/10.1029/2009JB006716.

Fischer, K.M., Hawman, R.B., Wagner, L.S., 2010. Southeastern suture of the appalachian margin experiment. URL: https://doi.org/10.7914/SN/Z9_2010.

Foley, B.J., Long, M.D., 2011. Upper and mid–mantle anisotropy beneath the Tonga slab. Geophysical Research Letters 38. URL: https://doi.org/10.1029/2010GL046021.

Fontaine, F.R., Barruol, G., Tommasi, A., Bokelmann, G.H.R., 2007. Upper-mantle flow beneath French Polynesia from shear wave splitting. Geophysical Journal International 170, 1262–1288. URL: https://doi.org/10.1111/j.1365-246X.2007.03475.x.

Frost, D.A., Romanowicz, B., Roecker, S., 2020. Upper mantle slab under Alaska: contribution to anomalous core-phase observations on south-Sandwich to Alaska paths. Physics of the Earth and Planetary Interiors 299, 106427. URL: https://doi.org/10.1016/j.pepi.2020.106427.

Frost, D.A., Rost, S., Selby, N., Stuart, G., 2013. Detection of a tall ridge at the core-mantle boundary from scattered PKP energy. Geophys. J. Int. 195. URL: https://doi.org/10.1093/gji/ggt242.

Gary Pavlis, Hersh Gilbert, 2011. Ozark illinois indiana kentucky (oiink) flexible array experiment. URL: https://doi.org/10.7914/SN/XO_2011.

Graw, J.H., Hansen, S.E., 2017. Upper mantle seismic anisotropy beneath the northern transantarctic mountains, antarctica from pks, sks, and skks splitting analysis. Geochemistry, Geophysics, Geosystems 18, 544–557. URL: https://doi.org/10.1002/2016GC006729.

Grund, M., Ritter, J.R., 2018. Widespread seismic anisotropy in Earth's lowermost mantle beneath the Atlantic and Siberia. Geology 47, 123–126. URL: https://doi.org/10.1130/G45514.1.

He, X., Long, M.D., 2011. Lowermost mantle anisotropy beneath the northwestern Pacific: Evidence from PcS, ScS, SKS, and SKKS phases. Geochemistry, Geophysics, Geosystems 12, Q12012. URL: https://doi.org/10.1029/2011GC003779.

IRIS DMC, 2012. Data Services Products: SWS-DBs Shear-wave splitting databases. URL: https://doi.org/10.17611/DP/SWS.1.

IRIS Transportable Array, 2003. USArray Transportable Array. URL: https://www.fdsn.org/networks/detail/TA/, doi:10.7914/SN/TA.

Kawai, K., Geller, R.J., 2010. Waveform inversion for localized seismic structure and an application to D" structure beneath the Pacific. Journal of Geophysical Research: Solid Earth 115. URL: https://doi.org/10.1029/2009JB006503.

Lamont Doherty Earth Observatory (LDEO), Columbia University, 1970. Lamont-doherty cooperative seismographic network. URL: https://doi.org/10.7914/SN/LD.

Leng, K., Nissen-Meyer, T., van Driel, M., 2016. Efficient global wave propagation adapted to 3-D structural complexity: a pseudospectral/spectral-element approach. Geophysical Journal International 207, 1700–1721. URL: https://doi.org/10.1093/gji/ggw363.

Leng, K., Nissen-Meyer, T., van Driel, M., Hosseini, K., Al-Attar, D., 2019. AxiSEM3D: broad-band seismic wavefields in 3-D global earth models with undulating discontinuities. Geophysical Journal International 217, 2125–2146. URL: https://doi.org/10.1093/gji/ggz092.

Levin, V., Park, J., 1997. P-SH conversions in a flat-layered medium with anisotropy of arbitrary orientation. Geophysical Journal International 131, 253–266. URL: https://doi.org/10.1111/j.1365-246X.1997.tb01220.x.

Liu, C., Grand, S.P., 2018. Seismic attenuation in the African LLSVP estimated from PcS phases. Earth and Planetary Science Letters 489, 8–16. URL: https://doi.org/10.1016/j.epsl.2018.02.023.

Liu, K., Elsheikh, A., Lemnifi, A., Purevsuren, U., Ray, M., Refayee, H., Yang, B., yu, Y., Gao, S., 2014. A uniform database of teleseismic shear wave splitting measurements for the western and central United States. Geochemistry, Geophysics, Geosystems 15, 2075–2085. URL: https://doi.org/10.1002/2014GC005267.

Long, M.D., Becker, T., 2010. Mantle dynamics and seismic anisotropy. Earth and Planetary Science Letters 297, 341–354. URL: https://doi.org/10.1016/j.epsl.2010.06.036.

Long, M.D., Silver, P.G., 2009. Shear Wave Splitting and Mantle Anisotropy: Measurements, Interpretations, and New Directions. Surveys in Geophysics 30, 407–461. URL: https://doi.org/10.1007/s10712-009-9075-1.

Long, M.D., van der Hilst, R.D., 2005. Upper mantle anisotropy beneath japan from shear wave splitting. Physics of the Earth and Planetary Interiors 151, 206–222. URL: https://doi.org/10.1016/j.pepi.2005.03.003.

Lopes, E., Long, M.D., Karabinos, P., Aragon, J.C., 2020. SKS Splitting and Upper Mantle Anisotropy Beneath the Southern New England Appalachians: Constraints From the Dense SEISConn Array. Geochemistry, Geophysics, Geosystems 21, e2020GC009401. URL: https://doi.org/10.1029/2020GC009401.

Lutz, K., Long, M., Creasy, N., Deng, J., 2020. Seismic anisotropy in the lowermost mantle beneath North America from SKS-SKKS splitting intensity discrepancies. Physics of the Earth and Planetary Interiors 305, 106504. URL: https://doi.org/10.1016/j.pepi.2020.106504.

Lynner, C., 2021. Anisotropy-revealed change in hydration along the Alaska subduction zone. Geology 49, 1122–1125. URL: https://doi.org/10.1130/G48860.1.

Lynner, C., Long, M.D., 2013. Sub-slab seismic anisotropy and mantle flow beneath the caribbean and scotia subduction zones: Effects of slab morphology and kinematics. Earth and Planetary Science Letters 361, 367–378. URL: https://doi.org/10.1016/j.epsl.2012.11.007.

Lynner, C., Long, M.D., 2015. Heterogeneous seismic anisotropy in the transition zone and uppermost lower mantle: evidence from South America, Izu-Bonin and Japan. Geophysical Journal International 201, 1545–1552. URL: https://doi.org/10.1093/gji/ggv099.

Mohiuddin, A., D. Long, M., Lynner, C., 2015. Mid-mantle seismic anisotropy beneath Southwestern Pacific subduction systems and implications

for mid-mantle deformation. Physics of the Earth and Planetary Interiors 245. URL: https://doi.org/10.1016/j.pepi.2015.05.003.

Murdie, R.E., Russo, R.M., 1999. Seismic anisotropy in the region of the chile margin triple junction. Journal of South American Earth Sciences 12, 261–270. URL: https://doi.org/10.1016/S0895-9811(99)00018-8.

Natural Resources Canada (NRCAN Canada), 1975. Canadian national seismograph network. URL: https://doi.org/10.7914/SN/CN.

Nikulin, A., Levin, V., Park, J., 2009. Receiver function study of the cascadia megathrust: Evidence for localized serpentinization. Geochemistry, Geophysics, Geosystems 10. URL: https://doi.org/10.1029/2009GC002376.

Nissen-Meyer, T., van Driel, M., Stähler, S.C., Hosseini, K., Hempel, S., Auer, L., Colombi, A., Fournier, A., 2014. AxiSEM: broadband 3-D seismic wavefields in axisymmetric media. Solid Earth 5, 425–445. URL: https://doi.org/10.5194/se-5-425-2014.

Niu, F., Perez, A.M., 2004. Seismic anisotropy in the lower mantle: A comparison of waveform splitting of SKS and SKKS. Geophysical Research Letters 31. URL: https://doi.org/10.1029/2004GL021196.

Northern California Earthquake Data Center, 2014. Berkeley digital seismic network (bdsn). URL: https://doi.org/10.7932/BDSN.

Nowacki, A., Wookey, J., Kendall, J.M., 2010. Deformation of the lowermost mantle from seismic anisotropy. Nature 467, 1091–1094. URL: https://doi.org/10.1038/nature09507.

Panning, M., Romanowicz, B., 2006. A three-dimensional radially anisotropic model of shear velocity in the whole mantle. Geophysical Journal International 167, 361–379. URL: https://doi.org/10.1111/j.1365-246X.2006.03100.x.

Panning, M.P., Nolet, G., 2008. Surface wave tomography for azimuthal anisotropy in a strongly reduced parameter space. Geophysical Journal International 174, 629–648. URL: https://doi.org/10.1111/j.1365-246X.2008.03833.x.

Penn State University, 2004. Pennsylvania state seismic network. URL: https://doi.org/10.7914/SN/PE.

Reiss, M., Rümpker, G., 2017. SplitRacer: MATLAB Code and GUI for Semiautomated Analysis and Interpretation of Teleseismic Shear-Wave Splitting. Seismological Research Letters 88, 392 — 409. URL: https://doi.org/10.1785/0220160191.

Reiss, M.C., Long, M.D., Creasy, N., 2019. Lowermost Mantle Anisotropy Beneath Africa From Differential SKS-SKKS Shear-Wave Splitting. Journal of Geophysical Research: Solid Earth 124, 8540–8564. URL: https://doi.org/10.1029/2018JB017160.

Rost, S., Thomas, C., 2009. Improving Seismic Resolution Through Array Processing Techniques. Surveys in Geophysics 30, 271–299. URL: https://doi.org/10.1007/s10712-009-9070-6.

Russo, R.M., Silver, P.G., 1994. Trench-Parallel Flow Beneath the Nazca

Plate from Seismic Anisotropy. Science 263, 1105–1111. URL: https://doi.org/10.1126/science.263.5150.1105.

Savage, M.K., 1999. Seismic anisotropy and mantle deformation: What have we learned from shear wave splitting? Reviews of Geophysics 37, 65 – 106. URL: https://doi.org/10.1016/10.1029/98RG02075.

Schulte-Pelkum, V., Monsalve, G., Sheehan, A., Pandey, M., Sapkota, S., Bilham, R., Wu, F., 2005. Imaging the indian subcontinent beneath the himalaya. Nature 435, 1222–1225.

Scripps Institution of Oceanography, 1986. Global seismograph network - iris/ida. URL: https://doi.org/10.7914/SN/II.

Selby, N.D., 2008. Application of a generalized F detector at a seismometer array. Bull. seism. Soc. Am. 98, 2469–2481. URL: https://doi.org/10.1785/0120070282.

Silver, P.G., 1996. Seismic Anisotropy beneath the Continents: Probing the Depths of Geology. Annual Review of Earth and Planetary Sciences 24, 385 – 432. URL: https://doi.org/10.1146/annurev.earth.24.1.385.

Silver, P.G., Chan, W.W., 1991. Shear wave splitting and subcontinental mantle deformation. Journal of Geophysical Research: Solid Earth 96, 16429–16454. URL: https://doi.org/10.1029/91JB00899.

Simon Klemperer, Kate Miller, 2010. Flexarray 3d passive seismic imaging of core-complex extension in the ruby range nevada. URL: https://doi.org/10.7914/SN/YX_2010.

Su, L., Park, J., 1994. Anisotropy and the splitting of ps waves. Physics of the Earth and Planetary Interiors 86, 263–276. URL: https://doi.org/10.1016/0031-9201(94)90125-2.

Suzuki, Y., Kawai, K., Geller, R.J., 2021. Imaging paleoslabs and inferring the Clapeyron slope in D" beneath the northern Pacific based on high-resolution inversion of seismic waveforms for 3-D transversely isotropic structure. Physics of the Earth and Planetary Interiors , 106751URL: https://doi.org/10.1016/j.pepi.2021.106751.

Tesoniero, A., Leng, K., D.Long, M., Nissen-Meyer, T., 2020. Full wave sensitivity of SK(K)S phases to arbitrary anisotropy in the upper and lower mantle. Geophysical Journal International 222, 412 – 435. URL: https://doi.org/10.1093/gji/ggaa171.

UC San Diego, 1982. Anza regional network. URL: https://doi.org/10.7914/SN/AZ.

University of Oregon, 1990. Pacific northwest seismic network - university of oregon. URL: https://doi.org/10.7914/SN/UO.

University of Washington, 1963. Pacific northwest seismic network - university of washington. URL: https://doi.org/10.7914/SN/UW.

Vinnik, L., Farra, V., Romanowicz, B., 1989. Observational evidence for diffracted SV in the shadow of the Earth's core. Geophysical Research Letters - GEOPHYS RES LETT 16, 519–522. URL: https://doi.org/GL016i006p00519.

Vinnik, L., Romanowicz, B., Le Stunff, Y., Makeyeva, L., 1995. Seismic anisotropy in the D" layer. Geophysical Research Letters 22, 1657–1660. URL: https://doi.org/10.1029/95GL01327.

Walker, A., Wookey, J., 2012. MSAT - a new toolkit for the analysis of elastic and seismic anisotropy. Computers and Geosciences 49, 81–90. URL: https://doi.org/10.1016/j.cageo.2012.05.031.

Walpole, J., Wookey, J., Kendall, J.M., Masters, T.G., 2017. Seismic anisotropy and mantle flow below subducting slabs. Earth and Planetary Science Letters 465, 155–167. URL: https://doi.org/10.1016/j.epsl.2017.02.023.

Walpole, J., Wookey, J., Masters, G., Kendall, J.M., 2014. A uniformly processed data set of SKS shear wave splitting measurements: A global investigation of upper mantle anisotropy beneath seismic stations. Geochemistry, Geophysics, Geosystems 15, 1991–2010. URL: https://doi.org/10.1002/2014GC005278.

Walsh, E., Arnold, R., Savage, M.K., 2013. Silver and Chan revisited. Journal of Geophysical Research: Solid Earth 118, 5500–5515. URL: https://doi.org/10.1002/jgrb.50386.

Wessel, P., Smith, W.H.F., 1998. New, improved version of generic mapping tools released. Eos, Transactions American Geophysical Union 79, 579–579. URL: https://doi.org/10.1029/98EO00426.

Wirth, E.A., Long, M.D., 2012. Multiple layers of seismic anisotropy and a low-velocity region in the mantle wedge beneath japan: Evidence from

teleseismic receiver functions. Geochemistry, Geophysics, Geosystems 13. URL: https://doi.org/10.1029/2012GC004180.

Wolf, J., Creasy, N., Pisconti, A., Long, M.D., Thomas, C., 2019. An investigation of seismic anisotropy in the lowermost mantle beneath Iceland. Geophysical Journal International 219, S152 – S166. URL: https://doi.org/10.1093/gji/ggz312.

Wolf, J., Frost, D.A., Long, M.D., Garnero, E., Aderoju, A.O., Creasy, N., Bozdağ, E., 2023a. Observations of Mantle Seismic Anisotropy Using Array Techniques: Shear-Wave Splitting of Beamformed SmKS Phases. Journal of Geophysical Research: Solid Earth 128, e2022JB025556. URL: https://doi.org/10.1029/2022JB025556.

Wolf, J., Long, M.D., 2022. Slab-driven flow at the base of the mantle beneath the northeastern pacific ocean. Earth and Planetary Science Letters 594, 117758. URL: https://doi.org/10.1016/j.epsl.2022.117758.

Wolf, J., Long, M.D., 2023a. Lowermost mantle structure beneath the central Pacific Ocean: ultra-low velocity zones and seismic anisotropy. Authorea URL: https://doi.org/10.22541/essoar.168286631.17963195/v1.

Wolf, J., Long, M.D., 2023b. Upper mantle anisotropy and flow beneath the Pacific Ocean revealed by differential PS-SKS splitting. Authorea URL: https://doi.org/10.22541/essoar.168319873.31441797/v1.

Wolf, J., Long, M.D., Creasy, N., Garnero, E., 2023b. On the measurement of Sdiff splitting caused by lowermost mantle anisotropy. Geophysical Journal International URL: https://doi.org/10.1093/gji/ggac490.

Wolf, J., Long, M.D., Leng, K., Nissen-Meyer, T., 2022a. Constraining deep mantle anisotropy with shear wave splitting measurements: Challenges and new measurement strategies. Geophysical Journal International 230, 507–527. URL: https://doi.org/10.1093/gji/ggac055.

Wolf, J., Long, M.D., Leng, K., Nissen-Meyer, T., 2022b. Sensitivity of SK(K)S and ScS phases to heterogeneous anisotropy in the lowermost mantle from global wavefield simulations. Geophysical Journal International 228, 366–386. URL: https://doi.org/10.1093/gji/ggab347.

Wolfe, C.J., Silver, P.G., 1998. Seismic anisotropy of oceanic upper mantle: Shear wave splitting methodologies and observations. Journal of Geophysical Research: Solid Earth 103, 749–771. URL: https://doi.org/10.1029/97JB02023.

Wookey, J., Kendall, J.M., Rümpker, G., 2005. Lowermost mantle anisotropy beneath the north Pacific from differential S-ScS splitting. Geophysical Journal International 161, 829–838. URL: https://doi.org/10.1111/j.1365-246X.2005.02623.x.

Yuan, K., Beghein, C., 2014. Three-dimensional variations in Love and Rayleigh wave azimuthal anisotropy for the upper 800km of the mantle. Journal of Geophysical Research: Solid Earth 119, 3232–3255. URL: https://doi.org/10.1002/2013JB010853.

Zhu, H., Yang, J., Li, X., 2020. Azimuthal Anisotropy of the North American Upper Mantle Based on Full Waveform Inversion. Journal of Geophysical

Research: Solid Earth 125, e2019JB018432. URL: https://doi.org/10.1029/2019JB018432.

Zietlow, D.W., Sheehan, A.F., Molnar, P.H., Savage, M.K., Hirth, G., Collins, J.A., Hager, B.H., 2014. Upper mantle seismic anisotropy at a strike-slip boundary: South Island, New Zealand. Journal of Geophysical Research: Solid Earth 119, 1020–1040. URL: https://doi.org/10.1002/2013JB010676.